Supplemental Information

Quantifying Dynamics in Phase-Separated Condensates Using Fluorescence Recovery after Photobleaching

Nicole O. Taylor, Ming-Tzo Wei, Howard A. Stone, and Clifford P. Brangwynne

Quantifying dynamics in phase-separated protein condensates using fluorescence recovery after photobleaching

N.O. Taylor[1], MT Wei[1], H.A. Stone[2*], C.P. Brangwynne[1*]

1. Princeton University, Department of Chemical and Biological Engineering, Princeton, NJ

2. Princeton University, Department of Mechanical and Aerospace Engineering, Princeton, NJ

*correspondence: cbrangwy@princeton.edu, hastone@princeton.edu

Supplementary Methods

Mathematical Models for FRAP Analysis: Large Drops

To describe the fluorophore concentration profiles in a FRAP experiment inside large drops, we tested two commonly used models. The first model assumes that the concentration of fluorescent molecules at the bleach spot boundary is fixed during the entire recovery process, i.e., $C(R,t) = C(R,0) = C_1$, a constant. Equivalently, it assumes that the normalized concentration, $C^*(r,t) = (C(r,t) - C(r,0))/(C_1 - C(r,0))$, equals one at the boundary, $C^*(R,t) = 1$. Supplementary Table 1 displays the equations for the concentration profiles in 1D (cartesian), 2D (cylindrical), and 3D (spherical), which are solutions to the diffusion equation $\partial C^*/\partial t = D\nabla^2 C^*$, where ∇^2 is the Laplacian. The second model assumes that diffusion occurs in an infinite medium, i.e., the normalized concentration far from the bleach spot is fixed, $C^*(\infty, t) = 1$. Here, C^* is defined as $C^*(r,t) = (C(r,t) - C(r,0))/(C(\infty,t) - C(r,0))$. Supplementary Table 3 displays the equations for the concentration profiles in 1D (cartesian), 2D (cylindrical), and 3D (spherical). The concentration profiles are then integrated using the equations S1-S3 (for cartesian, cylindrical, and spherical coordinates respectively), yielding the average normalized concentration in Supplementary Table 2 and Table 2 in the main text.

The average fluorescence recovery reported in the main text results from averaging in the 2D imaging plane. However, the data are compared in the main text to the 3D infinite model averaged in the 3D volume. We sought to determine whether averaging the 3D infinite model in the 2D plane would result in any significant difference. The 3D infinite equation in Supplementary Table 3 row 3 was also averaged in the 2D plane using Eq. S2, resulting in Eq. S4. Predicted average fluorescence recovery in a 2D plane versus 3D volume of a sphere is very similar (Fig. S3). Moreover, using this 2D average led to no significant change or improvement in the R^2 or measured diffusivities (Supplementary Table 4).

$$\langle C^* \rangle(t) = \int_{-R}^{R} C^*(x,t)dx \, / \int_{-R}^{R} dx \tag{S1}$$

$$\langle C^* \rangle(t) = \int_{0}^{R} C^*(r,t)rdr \, / \int_{0}^{R} rdr \tag{S2}$$

$$\langle C^* \rangle(t) = \int_0^R C^*(r,t) r^2 dr \,/\, \int_0^R r^2 dr \tag{S3}$$

$$\langle C^* \rangle(t) = 1 + 2\left(\frac{t}{\pi\tau}\right)^{1/2} - 2\left(\frac{t}{\pi\tau}\right)^{1/2} exp(-\tau/(4t)) -$$
$$erf\left(\left(\frac{\tau}{4t}\right)^{1/2}\right) + 2(t/\tau)erf\left(\left(\frac{\tau}{4t}\right)^{1/2}\right) - (t/\tau)erf\left(\left(\frac{\tau}{t}\right)^{1/2}\right) \tag{S4}$$

Supplementary Table 1: Fixed boundary solutions
Expressions for the normalized concentration for a 1D (cartesian), 2D (cylindrical), and 3D (spherical) FRAP model with concentration fixed at the bleach spot boundary, $x = R$ in cartesian and $r = R$ in cylindrical and spherical coordinates, see also (1). J_0 and J_1 are Bessel functions of the first kind of order zero and one, respectively. $\tau = R^2/D$ for all models.

Type	Concentration
1D Pure Diffusion (Fixed)	$C^*(x,t) = 1 - \sum_{n=0}^{\infty} \frac{4(-1)^n}{(2n+1)\pi} \exp\left(-\left((2n+1)\pi\right)^2 t/(4\tau)\right) \cos\left((2n+1)\pi x/(2R)\right)$
2D Pure Diffusion (Fixed)	$C^*(r,t) = 1 - \sum_{n=1}^{\infty} \frac{2J_0(\alpha_n r)}{(\alpha_n R)J_1(\alpha_n R)} \exp(-(\alpha_n R)^2 t/\tau)$ with $J_0(\alpha_n R) = 0$
3D Pure Diffusion (Fixed)	$C^*(r,t) = 1 + \sum_{n=1}^{\infty} \frac{2(-1)^n \sin(n\pi r/R)}{n\pi(r/R)} \exp(-(n\pi)^2 t/\tau)$

Supplementary Table 2. Expressions for the average normalized concentration for fixed boundary models in 1D (cartesian), 2D (cylindrical), and 3D (spherical), a simple exponential model, and a reaction-dominant recovery model. For fixed boundary models, $<C^*>(t)$ was calculated by averaging the expressions given in Supplementary Table 1. Leading order refers to the first term in the summation, which is a good approximation at long times. J_o is the Bessel function of the first kind of order zero.* (2)

Type	Equation	Leading Order
1D Pure Diffusion (Fixed)	$\langle C^* \rangle(t) = 1 - \sum_{n=0}^{\infty} \frac{8}{((2n+1)\pi)^2} \exp\left(-((2n+1)\pi)^2 t/(4\tau)\right)$	$\langle C^* \rangle(t) \approx 1 - 0.8\exp(-2.5t/\tau)$
2D Pure Diffusion (Fixed)	$\langle C^* \rangle(t) = 1 - \sum_{n=1}^{\infty} \frac{4}{(\alpha_n R)^2} \exp(-(\alpha_n R)^2 t/\tau)$ with $J_0(\alpha_n R) = 0$	$\langle C^* \rangle(t) \approx 1 - 0.7\exp(-5.8t/\tau)$
3D Pure Diffusion (Fixed)	$\langle C^* \rangle(t) = 1 - \sum_{n=1}^{\infty} \frac{6}{(n\pi)^2} \exp(-(n\pi)^2 t/\tau)$	$\langle C^* \rangle(t) \approx 1 - 0.6\exp(-10t/\tau)$
Simple Exponential	$\langle C^* \rangle(t) = A(1 - \exp(-t/\tau))$	N/A
*Reaction	$\langle C^* \rangle(t) = 1 - C_{eq}\exp(-k_{off}t)$	N/A

Supplementary Table 3: Infinite boundary solutions
Expressions for the normalized concentration for a 1D (cartesian), 2D (cylindrical), and 3D (spherical) FRAP model with infinite boundaries, see also (1). The error function and order zero modified Bessel function are denoted by *erf* and I_0, respectively. $\tau = R^2/D$ for all models.

Type	Concentration
1D Pure Diffusion (Infinite boundary)	$C^*(x,t) = 1 - \frac{1}{2}\left\{\mathrm{erf}\left(\frac{1-x/R}{2(t/\tau)^{1/2}}\right) + \mathrm{erf}\left(\frac{1+x/R}{2(t/\tau)^{1/2}}\right)\right\}$
2D Pure Diffusion (Infinite boundary)	$C^*(r,t) = 1 - \frac{\tau}{2R^2 t}\exp\left(-\frac{(r/R)^2\tau}{4t}\right)\int_0^R \exp\left(-\frac{(s/R)^2\tau}{4t}\right) I_0\left(\frac{rs\tau}{2R^2 t}\right) s\,ds$
3D Pure Diffusion (Infinite boundary)	$C^*(r,t) = 1 - \frac{1}{2}\left\{\mathrm{erf}\left(\frac{1-r/R}{2\left(\frac{t}{\tau}\right)^{1/2}}\right) + \mathrm{erf}\left(\frac{1+r/R}{2\left(\frac{t}{\tau}\right)^{1/2}}\right)\right\} + \frac{R}{r}\left(\frac{t}{\pi\tau}\right)^{1/2}\left\{\exp\left(-\frac{(1-r/R)^2\tau}{4t}\right) - \right.$

$$\exp\left(-\frac{(1+r/R)^2\tau}{4t}\right)\Big\}$$

Supplementary Table 4: Summary of sum of squared residuals, R^2, and D from model fits (Eq. S4 and Table 2 row 2-3) to LAF-1 data in Fig. S3.

Model fit	Average type	Σ **Residuals**^{2}	R^2	$Dx10^3$ ($\mu m^2/s$)
3D Infinite non-step	2D	0.032	0.97	1.7
3D Infinite non-step	3D	0.018	0.98	1.7
3D Infinite	2D	0.014	0.99	1.4
3D Infinite	3D	0.003	0.99	1.2
2D Infinite	2D	0.001	0.99	2.6

Supplementary Table 5. Summary of sum of squared residuals and R^2 from model fits to LAF-1 data in Fig. 7A.

Model fit	Σ **Residuals**^{2}	R^2
Exp	0.034	0.97
1D Infinite	0.025	0.97
3D Infinite non-step	0.018	0.98
3D Fixed	0.010	0.99
3D Infinite	0.003	0.99
2D Infinite	0.001	0.99

3D Non-step Initial Condition Model

FRAP experiments with non-step initial bleaching profiles were modeled in two equivalent ways, as described in the Results section of the main text. In the first method, normalized initial concentration profiles for data measured using a 3 µm ROI (i.e., spherical initial shape) are fit to the 3D infinite model equation (Supplementary Table 2, row 3) to obtain $t_s^* = t_s/\tau$ and a new initial condition defined by $C^*(r,t_s^*)$. The solution for a semi-infinite sphere with arbitrary initial condition is well-known from the literature (3) and is

$$C^*(r,t) = \frac{1}{2rR(\pi t/\tau)^{1/2}}\int_0^\infty C^*(r',t_s/\tau)r'dr'\left[exp\left(-\frac{(r-r\prime)^2}{4R^2t/\tau}\right)-exp\left(-\frac{(r+r\prime)^2}{4R^2t/\tau}\right)\right] \qquad (S5)$$

Integration of Eq. S5 following Eq. S3 with $C^*(r',t_s/\tau)$ evaluated using Supplementary Table 3, row 3, gives

$$\langle C^*\rangle(t) =$$
$$1 + \frac{6t_s(t_s+t)^{1/2}}{\tau^{3/2}(\pi)^{1/2}}\left[exp\left(-\frac{\tau}{t_s+t}\right)-1\right] + 3(t_s/\tau)erf\left(\frac{\tau^{1/2}}{(t_s+t)^{1/2}}\right) -$$

4

$$\frac{3}{4R^4(\pi t/\tau)^{1/2}}\int_0^R r\,dr \int_0^\infty r'dr'\left[erf\left(\frac{1+r\prime/R}{2(t_s/\tau)^{1/2}}\right)+erf\left(\frac{1-r\prime/R}{2(t_s/\tau)^{1/2}}\right)\right]\left[exp\left(-\frac{(r-r\prime)^2}{4R^2t/\tau}\right)-\right.$$
$$\left.exp\left(-\frac{(r+r\prime)^2}{4R^2t/\tau}\right)\right] \tag{S6}$$

For non-step initial conditions (i.e., $t_s \neq 0$), $<C^*>(0)$ in Eq. S6 is not equal to zero. Thus, to compare our data which is normalized such that $<C^*>(0) = 0$, we re-normalize the model equation before fitting to obtain $\langle C^*_{fit}\rangle(t)$.

$$\langle C^*_{fit}\rangle(t) = (\langle C^*\rangle(t) - \langle C^*\rangle(0))/(1 - \langle C^*\rangle(0)) \tag{S7}$$

The second method can be used for data fit to the 3D, 2D, and 1D infinite model equations. Rather than use $C^*(r', t_s/\tau)$ in Eq. S5, t is replaced with $t_s + t$ in the equations in Table 2 of the main text. As an example, using this substitution in the 3D infinite model leads to Eq. S8.

$$\langle C^*\rangle(t) = 1 - erf\left(\frac{\tau^{1/2}}{(t_s+t)^{1/2}}\right)+\frac{\tau^{1/2}}{\pi^{1/2}(t_s+t)^{1/2}}\left[3-exp\left(-\frac{\tau}{t_s+t}\right)\right]+2\frac{(t_s+t)^{3/2}}{\pi^{1/2}\tau^{3/2}}\left[exp\left(-\frac{\tau}{t_s+t}\right)-1\right] \tag{S8}$$

Again, for non-step initial conditions (i.e., $t_s \neq 0$), $<C^*>(0)$ in Eq. S8 is not equal to zero and we use Eq. S7 to re-normalize the model equation before fitting the data. The same procedure was used when fitting data to the 2D and 1D infinite models with non-step initial conditions.

3D Cylindrical Model

To determine quantitatively whether one expects quasi-1D or quasi-2D dynamics for bleach ROIs of 50 and 1 μm (Fig. 8A), respectively, we compared $<C^*>$ dynamics of 1D and 2D Infinite models to a 3D cylindrical model in an infinite medium with different aspect ratios of the geometry. The solution for a cylindrical source was shown previously by Penkova et al. (4) and can be rewritten for a cylindrical sink (i.e., concentration within the cylinder is lower than outside) with concentration normalized as

$$C(r,z,t) = 1 - \frac{1}{2}\left\{erf\left(\frac{z+a}{(4Dt)^{1/2}}\right)-erf\left(\frac{z-a}{(4Dt)^{1/2}}\right)\right\}+\frac{1}{2}\left\{erf\left(\frac{z+a}{(4Dt)^{1/2}}\right)-erf\left(\frac{z-a}{(4Dt)^{1/2}}\right)\right\}\times$$
$$exp\left(-\frac{(r^2+b^2)}{4Dt}\right)\sum_{n=0}^\infty\left(\frac{r^2}{4Dt}\right)^n\frac{1}{n!}\sum_{k=0}^n\left(\frac{b^2}{4Dt}\right)^k\frac{1}{k!} \tag{S9}$$

where a and b are the half height and radii of the cylinder, respectively, r and z are the radial and axial coordinates, respectively, and D is the diffusion coefficient. To simplify Eq. S9 we define dimensionless variables $t^* = t/(b^2/D)$, $\delta = a/b, r^* = r/b$, $z^* = z/b$. Since our FRAP measurements, and thus $<C^*>$, are performed at the $z = 0$ plane, we also evaluate Eq. S9 at the $z = 0$ plane. These simplifications result in:

$$C(r^*,0,t^*) =$$
$$1 - erf\left(\frac{\delta}{(4t^*)^{1/2}}\right)+erf\left(\frac{\delta}{(4t^*)^{1/2}}\right)\times exp\left(-\frac{(r^{*2}+1)}{4t^*}\right)\sum_{n=0}^\infty\left(\frac{r^{*2}}{4t^*}\right)^n\frac{1}{n!}\sum_{k=0}^n\left(\frac{1}{4t^*}\right)^k\frac{1}{k!}$$
$$(S10)$$

Integration of Eq. S10 using the formula in Eq. S2 results in:

$$\langle C(r^*, 0, t^*) \rangle = 1 - erf\left(\frac{\delta}{(4t^*)^{1/2}}\right) + 4erf\left(\frac{\delta}{(4t^*)^{1/2}}\right) t^* \sum_{n=0}^{\infty} \frac{1}{n!} \frac{\Gamma(1+n) - \Gamma(1+n, 1/(4t^*))}{\Gamma(1+n)} \Gamma(1 + n, 1/(4t^*))$$

(S11)

where $\Gamma(1+n)$ is the complete gamma function, $\Gamma(1+n) = \int_0^{\infty} t^n exp(-t)dt = n!$, and $\Gamma(1+n, 1/(4t^*))$ is the incomplete gamma function, $\Gamma(1+n, 1/(4t^*)) = \int_{1/(4t^*)}^{\infty} t^n exp(-t)dt$.

The value of δ required for achieving effectively quasi-1D diffusion was determined by evaluating $C^*(x, t)$ (Supplementary Table 3) at $x = 0$ and fitting δ in Eq. S11 (Fig. S5A). We evaluate the equation at $x = 0$ since in our experiment we only measure at the mid-plane but expect quasi-1D diffusion to occur along the axial dimension above and below the midplane. We determined δ required for quasi-2D diffusion by evaluating $\langle C^* \rangle(t)$ (Table 2 2D dimension) and fitting δ in Eq. S11 (Fig. S5A); we find that $\delta = 0.007$ (i.e pancake-shaped) and $\delta = 10.84$ (i.e. elongated cylinder) achieve effective 1D and 2D diffusion, respectively. These values are not experimentally obtainable for our system, however we can use $\delta = 0.1$ and 2.9, towards these shapes. Fig. S5B shows the comparison of the 3D cylindrical model using these parameters to 1D and 2D diffusion. For 2D diffusion, the models are similar, but begin noticeably deviating at roughly $<C^*> \sim 0.8$. For 1D diffusion they are also similar but significant deviations are noted even at $<C^*> \sim 0.6$. This suggests that FRAP data obtained using $\delta = 0.1$ and 2.9 can be reasonably well-fit to the 1D and 2D infinite models, respectively.

3D Finite Model: Local Equilibrium

To describe the fluorophore concentration profiles in a FRAP experiment inside drops where $R_{drop}/R_{bleach} = 1$, we developed a 3D spherically symmetric finite model. To describe the concentration profiles in each phase, we utilize the one-dimensional form of Fick's second law for the bleached concentration, C_b, in each phase in spherical coordinates.

$$\frac{\partial C_b(r,t)}{\partial t} = D\left(\frac{\partial^2 C_b}{\partial r^2} + \frac{2}{r}\frac{\partial C_b}{\partial r}\right) \quad r < R$$

(S12)

$$\frac{\partial C_b(r,t)}{\partial t} = D_+\left(\frac{\partial^2 C_b}{\partial r^2} + \frac{2}{r}\frac{\partial C_b}{\partial r}\right) \quad r > R$$

(S13)

Here, D and D_+ are the protein diffusion coefficients in the droplet and protein-lean phase, respectively, r is the spherical coordinate for diffusion, and R is the droplet and bleach radius (see Fig. 10A). Local equilibrium at the droplet-solution interface gives the boundary condition $C_b(R_-, t) = \alpha C_b(R_+, t)$, where α is the ratio of total protein concentration in the condensed phase to the protein-lean phase, and R_- and R_+ represent being just on the inside or outside of the droplet interface, respectively. Equating the mass fluxes at the droplet-solution interface gives the second boundary condition $D\partial C_b(R_-, t)/\partial r = D_+\partial C_b(R_+, t)/\partial r$. The third and fourth boundary conditions come from symmetry at the droplet center $\frac{\partial C_b(0,t)}{\partial r} = 0$ and assuming the protein-lean phase is an infinite sink such that $\lim_{r \to \infty} C_b(r, t) = 0$. The initial conditions in the droplet and protein-lean phases are $C_b(r, 0) = (1 - K)C_{d,in}$ for $r < R$ and $C_b(r, 0) = 0$ for

$r > R$. $C_{d,in}$ is the total protein concentration inside the droplet phase, which is constant over time, and *(1-K)* is the fraction of unbleached protein in the droplet phase. Accordingly, the fluorescent protein concentration, C_f, is found using the relationship $C_b + C_f = C_{d,in}$ for $r < R$ and $C_b + C_f = C_\infty$ for $r > R$, where C_∞ is the total protein concentration in the protein-lean phase.

To simplify Eqs. S12 and S13, we define dimensionless variables $t^* = t/\tau$, $\tau = R^2/D$, $\xi = r/R$, $\lambda = D_+/D$, and $\theta_b = C_b/[(1-K)C_d]$ and use the transformation $u = \theta_b \xi$. The resulting non-dimensional equations are

$$\frac{\partial u(\xi,t^*)}{\partial t^*} = \frac{\partial^2 u}{\partial \xi^2} \qquad \xi < 1 \tag{S14}$$

$$\frac{\partial u(\xi,t^*)}{\partial t^*} = \lambda \frac{\partial^2 u}{\partial \xi^2} \qquad \xi > 1 \tag{S15}$$

Eqs. S14 and S15 are solved subject to the non-dimensionalized boundary and initial conditions $u(1_-,t^*) = \alpha u(1_+,t^*)$, $\frac{\partial u(1_-,t^*)}{\partial \xi} - u(1_-,t^*) = \lambda\left[\frac{\partial u(1_+,t^*)}{\partial \xi} - u(1_+,t^*)\right]$, $u(0,t^*) = 0$, $\lim_{\xi \to \infty} u(\xi,t^*) = finite$, and $u(\xi,0) = \xi$ for $\xi < 1$ and $u(\xi,0) = 0$ for $\xi > 1$. We seek solutions using Laplace transforms of Eqs. S14 and S15 (with respect to t^*); Laplace transformed variables are indicated with the overbar, and s represents frequency in the Laplace domain:

$$s\bar{u} - \xi = \frac{\partial^2 \bar{u}}{\partial \xi^2} \qquad \xi < 1 \tag{S16}$$

$$s\bar{u} = \lambda \frac{\partial^2 \bar{u}}{\partial \xi^2} \qquad \xi > 1 \tag{S17}$$

where $-\xi$ in Eq. S16 comes from the initial condition, $u(\xi,0) = \xi$. Transformed boundary conditions are $\bar{u}(1_-,s) = \alpha \bar{u}(1_+,s)$, $\frac{\partial \bar{u}(1_-,s)}{\partial \xi} - \bar{u}(1_-,s) = \lambda\left[\frac{\partial \bar{u}(1_+,s)}{\partial \xi} - \bar{u}(1_+,s)\right]$, $\bar{u}(0,s) = 0$, and $\lim_{\xi \to \infty} \bar{u}(\xi,s) = finite$. The solutions in Laplace transform space to Eqs. S16 and S17 are

$$\overline{\theta_b}(\xi,s) = \frac{1}{s} - \frac{\left(\lambda + (s\lambda)^{1/2}\right)\sinh(s^{1/2}\xi)}{\alpha\xi s\{s^{1/2}\cosh(s^{1/2}) + \sinh(s^{1/2})[(s\lambda)^{1/2}/\alpha + \lambda/\alpha - 1]\}}$$
$$\xi < 1 \tag{S18}$$

$$\overline{\theta_b}(\xi,s) = \frac{exp[(s/\lambda)^{1/2}(1-\xi)]}{\xi\alpha s}\left[1 - \frac{\left(\lambda + (s\lambda)^{1/2}\right)\sinh(s^{1/2})}{\alpha\{s^{1/2}\cosh(s^{1/2}) + \sinh(s^{1/2})[(s\lambda)^{1/2}/\alpha + \lambda/\alpha - 1]\}}\right]$$
$$\xi > 1 \tag{S19}$$

Using the same approach as previously reported for the analogous heat transfer problem (5), we find the inverse Laplace transform of Eqs. S18 and S19 by using the Inversion Theorem for the Laplace transform (3):

$$\theta_b(\xi,t^*) = \frac{1}{2\pi i}\int_{\gamma - i\infty}^{\gamma + i\infty} \overline{\theta_b} exp(st^*)ds \tag{S20}$$

7

In Eqs. S18 and S19, $\overline{\theta_b}$ has a pole at $s = 0$ and a branch point at $s = 0$. Accordingly, we use the contour integral with a cut along the negative real axis (3) (Fig. S12) to obtain:

$$\theta_b(\xi, t^*) = \pi i\, Res[\overline{\theta_b}exp(st^*)] + \frac{1}{2\pi i}\int_0^\infty \overline{\theta_b}exp(st^*)ds - \frac{1}{2\pi i}\int_0^\infty \overline{\theta_b}exp(st^*)ds \tag{S21}$$

where the first integral corresponds to the contour FE and the second on the contour DC in Fig. S12. We set $s = \rho exp(i\pi)$ on FE and $s = \rho exp(-i\pi)$ on DC, giving $s^{1/2} = \rho^{1/2}i$ and $s^{1/2} = -\rho^{1/2}i$ on FE and DC, respectively. We find $Res[\overline{\theta_b}exp(st^*)] = 0$ by series expansion; substituting $\rho = u^2$ leads to:

$$\theta_b(\xi, t^*) = -\frac{2\alpha}{\pi\xi\lambda^{1/2}}\int_0^\infty du\, \frac{(u\cos(u) - \sin(u))\sin(u\xi)exp(-u^2 t^*)}{u^2[\sin(u)]^2 + \lambda\left[\frac{\alpha}{\lambda}(u\cos(u) - \sin(u)) + \sin(u)\right]^2} \qquad \xi < 1$$

(S22)

$$\theta_b(\xi, t^*) = -\frac{2}{\pi\xi\lambda^{1/2}}\int_0^\infty \frac{du}{u}\, \frac{(u\cos(u) - \sin(u))exp(-u^2 t^*)}{u^2[\sin(u)]^2 + \lambda\left[\frac{\alpha}{\lambda}(u\cos(u) - \sin(u)) + \sin(u)\right]^2} \times \left\{\cos\left(\frac{u^2}{\lambda^{1/2}}\left(1 - \frac{1}{\xi}\right)\right)\sin(u) + \lambda^{1/2}\sin\left(\frac{u}{\lambda^{1/2}}\left(1 - \frac{1}{\xi}\right)\right)\left[\frac{\alpha}{\lambda}(u\cos(u) - \sin(u)) + \sin(u)\right]\right\} \qquad \xi > 1 \quad (S23)$$

The normalized fluorescent concentration, $C^* = \frac{C_f - KC_{d,in}}{C_{d,in} - KC_{d,in}}$, inside the droplet is found using the condition $C_b + C_f = C_{d,in}$ and $\theta_b = C_b/[(1 - K)C_{d,in}]$, and is $C^* = 1 - \theta_b$. The average normalized fluorescence is found using $\langle C^*\rangle(t^*) = \int_0^1 C(r, t^*)\xi^2 d\xi \,/ \int_0^1 \xi^2 d\xi$, and after integration of the outer integral is

$$\langle C^*\rangle(t^*) = 1 - \frac{6\alpha}{\pi\lambda^{1/2}}\int_0^\infty du\, \frac{(u\cos(u) - \sin(u))^2 exp(-t^*)}{u^2\left\{u^2[\sin(u)]^2 + \lambda\left[\frac{\alpha}{\lambda}(u\cos(u) - \sin(u)) + \sin(u)\right]^2\right\}}$$

$$\xi < 1$$
(S24)

The integral in Eq. S24 was evaluated numerically using the integral function in Matlab, which uses global adaptive quadrature and we chose error tolerances typically of order 1×10^{-9}.

3D Finite Model: Interface Resistance

We found that fitting LAF-1 FRAP data using $R_{drop}/R_{bleach} = 1$ resulted in a diffusivity two orders of magnitude lower than expected (Fig. 11A) and hypothesized that this may result from resistance to mass transfer at the interface. We sought to estimate this resistance by using a mass transfer coefficient, k, and replacing the local equilibrium boundary condition by equating the mass flux on each side of the interface to that at the interface, $D\partial C(R_-, t)/\partial r = D_+\partial C(R_+, t)/\partial r = -k[C(R_-, t) - \alpha C(R_+, t)]$, see also (6). Thus, in the case of no resistance k approaches infinity and local equilibrium is established, $C(R_-, t) = \alpha C(R_+, t)$. As described in the previous section, we define dimensionless variables, use the transformation $u = \theta_b\xi$, and seek solutions using Laplace transforms. Transformed boundary conditions are $\partial\bar{u}(1_-, s)/\partial\xi - \bar{u}(1_-, s) = \lambda[\partial\bar{u}(1_+, s)/\partial\xi - \bar{u}(1_+, s)] = -k[\bar{u}(1_-, s) - \alpha\bar{u}(1_+, s)]$, $\partial\bar{u}(1_-, s)/\partial\xi - \bar{u}(1_-, s) = \lambda[\partial\bar{u}(1_+, s)/\partial\xi - \bar{u}(1_+, s)]$, $\bar{u}(0, s) = 0$, and $\lim_{\xi\to\infty}\bar{u}(\xi, s) = finite$. The solutions in Laplace space are

$$\overline{\theta_b}(\xi,s) =$$

$$\frac{1}{s} - \frac{k\left(\lambda+(s\lambda)^{1/2}\right)\sinh\left(s^{1/2}\xi\right)}{\alpha\xi s\left\{\cosh(s^{1/2})[s^{1/2}\lambda/\alpha+s^{1/2}k+s\lambda^{1/2}/\alpha]-\sinh(s^{1/2})\left[k-(\lambda/\alpha)(k-1)\left(1+(s/\lambda)^{1/2}\right)\right]\right\}}$$

$$\xi < 1 \quad \text{(S25)}$$

$$\overline{\theta_b}(\xi,s) = \frac{exp\left[(s/\lambda)^{1/2}(1-\xi)\right]}{\xi\alpha s}\left[\frac{k\left(s^{1/2}\cosh(s^{1/2})-\sinh(s^{1/2})\right)}{\cosh(s^{1/2})[s^{1/2}\lambda/\alpha+s^{1/2}k+s\lambda^{1/2}/\alpha]-\sinh(s^{1/2})\left[k-(\lambda/\alpha)(k-1)\left(1+(s/\lambda)^{1/2}\right)\right]}\right]$$

$$\xi > 1 \quad \text{(S26)}$$

In Eqs. S25 and S26, $\overline{\theta_b}$ has a pole at $s = 0$ and a branch point at $s = 0$. We again use the contour deformation (Fig. S12) (Eq. S21) with s rewritten in the same way. We again find $Res\left[\overline{\theta_b}exp(st^*)\right] = 0$ by series expansion; substituting $\rho = u^2$ leads to:

$$\theta_b(\xi,t^*) = -\frac{2\alpha k^2}{\pi\xi\lambda^{1/2}}\int_0^\infty du \frac{(u\cos(u)-\sin(u))\sin(u\xi)exp(-u^2t^*)}{u^2[u\cos(u)+(k-1)\sin(u)]^2+\lambda\left[\left(1+k\frac{\alpha}{\lambda}\right)u\cos(u)+\left(k-1-k\frac{\alpha}{\lambda}\right)\sin(u)\right]^2}$$

$$\xi < 1 \quad \text{(S27)}$$

Using the same equations described in the previous section, the average normalized fluorescence is

$$\langle C^*\rangle(t^*)$$
$$= 1-\frac{6\alpha k^2}{\pi\lambda^{1/2}}\int_0^\infty du \frac{(u\cos(u)-\sin(u))^2 exp(-u^2t^*)}{u^2\left\{u^2[u\cos(u)+(k-1)\sin(u)]^2+\lambda\left[\left(1+k\frac{\alpha}{\lambda}\right)u\cos(u)+\left(k-1-k\frac{\alpha}{\lambda}\right)\sin(u)\right]^2\right\}}$$

$$\xi < 1 \quad \text{(S28)}$$

The integral in Eq. S28 was again evaluated numerically using the integral function in Matlab and we chose error tolerances typically of order 1×10^{-9}. In the limit k approaches infinity, Eqs. S25-S28 reduce to Eqs. S18-S19, S22, and S24, respectively.

FRAP: 20 nm beads in 90% glycerol

The quantitative accuracy of using the 3D infinite non-step model was tested by performing a FRAP experiment where 20 nm in diameter red fluorescent beads in a 90% glycerol solution were bleached. The viscosity of 90% glycerol is known from literature; values range from $\mu = 0.219$ to $\mu = 0.235$ Pa.s at 20°C (7). Bead diffusion coefficient calculated from the Stokes-Einstein equation, $D_{bead} = k_B T/(6\pi\mu a)$, is 0.094 ± 0.003 μm^2/s, where a is bead radius, k_B is Boltzmann's constant, and T is temperature. Due to these fast diffusivities, we were unable to take z-stacks quickly enough to measure the 3D bleach shape inside a solution of 20 nm beads. Therefore, we estimated the bleach radius in the axial direction, r_z, by comparing the decrease in fluorescent intensity immediately after bleaching to that of LAF-1, for which we know r_z. For 20 nm beads, the fluorescence intensity decreases by 55% in the center of the bleach spot (i.e., $C(r = 0, t = 0)/C_0$), where C_0 is the intensity before bleaching. We measured a similar decrease in LAF-1 intensity (i.e., 50%) (Fig. 6A) which resulted in $r_z \sim 2$ μm. Therefore, we expect $r_z \sim 2$ μm for the bleach shape of the 20 nm bead solution, and since we measure $r_x = 2.05 \pm 0.13$ μm,

we estimate that the bleach shape is spherical. Accordingly, we used the 3D infinite model with non-step initial condition, resulting in $D = 0.066 \pm 0.025$ μm^2/s, which is just within error of the expected diffusivity. While using the 2D infinite model may yield a closer value to the diffusion coefficient predicted by Stokes-Einstein, the experimentally measured decrease in fluorescence after bleaching suggests that a 3D model better describes the recovery process. The slightly smaller measured apparent diffusion coefficient may arise from non-detectable aggregates of the 20 nm beads.

Fluorescence Correlation Spectroscopy Calibration

Diffusivity and concentration can be measured quantitatively using FCS, but first we require determination of the confocal volume experimentally. This is achieved by fitting FCS data of a sample with known diffusivity: Alexa 488 in water at 22°C has a diffusivity of 435 μm^2/s (8). We performed FCS experiments with a 30 s measurement time using a 60X oil immersion objective (Apo oil immersion, N.A. = 1.4, Nikon, Melville, NY) at concentrations between 1 and 50 nM either 1 μm or 4 μm above the coverslip. Data are fit to the autocorrelation function for simple diffusion with triplet-state kinetics, $G(\tau)$, is

$$G(\tau) = G(0) \frac{[1 - F + Fexp(-\tau/\tau_F)]}{1 - F} \frac{1}{[1 + \tau/\tau_D][1 + k^{-2}(\tau/\tau_D)^{1/2}]} \quad (S29)$$

where G(0) is the autocorrelation function at $\tau = 0$, F is the fraction of molecules entering the triplet state with characteristic relaxation time τ_F, $\tau_D = w_{xy}^2/4D$ is the diffusion time of Alexa 488 for the radial radii w_{xy} and diffusivity D, and $k = w_z/w_{xy}$ is the ratio of axial to radial radii of the measurement volume. Eq. S29 assumes that the measurement volume can be approximated as a three-dimensional Gaussian with the two parameters w_{xy} and w_z. A sample curve for 10 nM Alexa488 is shown in Fig. S13. Using Eq. S29 with known diffusivity and therefore τ_D, values of k and w_{xy} are obtained at 1 μm and 4 μm above the coverslip and are $k = 4.78 \pm 0.20$, $w_{xy} = 0.19 \pm 0.01$ and $k = 6.21 \pm 0.05$, $w_{xy} = 0.21 \pm 0.01$, respectively. Slightly different values of k and w_{xy} are found due to refractive index mismatch and detection volume distortion using an oil immersion objective (9, 10).

Determination of D_+ and C_∞ of LAF-1 using FCS

Autocorrelation data are obtained 4 μm above the coverslip by FCS over a 30 s measurement time (Fig. S14). We collect data at 4 μm rather than 1 μm above due to the presence of adsorbed protein at the surface. Diffusivity, D_+, and concentration of fluorophore-labeled LAF-1, C_{Dye}, in the protein-lean phase are determined using the parameters k and w_{xy} measured above and Eq. S29. C_∞ is then measured using the relation $C_\infty = C_{Dye}/(\%labeled)$, where %labeled is the labeled fraction of protein, determined by nanodrop. We use $k = 4.78 \pm 0.20$ and $w_{xy} = 0.19 \pm 0.01$ in Eq. S29, resulting in $D_+ = 94 \pm 11$ μm^2/s and $C_\infty = 2.2 \pm 1.3$ μM. Fitting using $k = 6.21 \pm 0.05$ and $w_{xy} = 0.21 \pm 0.01$ results in a 39% decrease and 28% increase in C_∞ and D_+, respectively.

Determination of $C_{d,in}$ and α of LAF-1 using FCS and Intensity Calibration

The ratio of protein concentration in the droplet to the protein-lean phase, α, can often be measured directly by the ratio of confocal intensities inside and out of droplets. However, surface adsorption of LAF-1 at the coverslip surface complicated this analysis and we were unable to reliably measure confocal intensity in the protein-lean phase. Instead, we determine α by measuring $C_{d,in}$ and C_∞ independently and dividing, $\alpha = C_{d,in}/C_\infty$. Due to the slow diffusion of LAF-1 inside droplets, we were unable to obtain accurate autocorrelation data and measure $C_{d,in}$ directly by commercial FCS. Instead, $C_{d,in}$ is determined in two steps. We first correlate the confocal intensity of the fluorophore used for labeling LAF-1, Dylight 488, to the measured concentration by FCS with 30 s measurement time (Fig. S15). The microscope laser power used to measure the intensity of the lower concentration (i.e., ~ 75 µW for 10-50 nM) Dylight488 solution necessary for FCS is different than that typically used to image LAF-1 droplets (i.e., ~ 0.9 µW). This is due to a much higher labeled LAF-1 concentration inside droplets. Using higher power (~75 µW) leads to saturation in intensity. Accordingly, the second step in determining $C_{d,in}$ is to measure the ratio of intensity at the high power used for a 10-50 nM Dylight solution to the intensity measured at the lower power used to image LAF-1 droplets. For this step, we use a solution of 500 nM Dylight 488 and obtained a correction factor, $cf = intensity@75\mu W / intensity@0.9\mu W = 67.7 +/-0.4$. The intensity of labeled LAF-1, I_{Dye}, expected using ~75 µW is calculated by multiplying by cf and converted to concentration, C_{Dye}, using the calibration curve in Fig. S15. $C_{d,in}$ is then measured using the relation $C_{d,in} = C_{Dye}/(\%labeled)$ and is 2.6 ± 1.2 mM. Division of $C_{d,in}$ by C_∞ gives $\alpha = 1189 \pm 880$. Laser power was measured after the 60x objective (Apo Oli immersion, N.A. 1.4, Nikon, Melville, NY) using a handheld digital power meter (PM100D Thorlabs, Newton, NJ) in scanning mode for a 512x512 field of view. We note that this measured concentration is significantly higher than that previously measured for LAF-1 droplets (11); this is partially explained by the lower salt concentration used in the present study, likely giving rise to slightly more concentrated droplets. Consistent with this, our measured D is an order of magnitude lower than that reported using FCS in droplets at 125 mM NaCl (11). Future studies may better reveal the reason behind this significant difference in dense phase concentration and diffusion coefficient.

Determination of D$_+$ of Ddx4-YFP using FCS

The diffusivity of Ddx4-YFP in the protein-lean phase is determined by FCS. We use the photon counting detector corresponding to a wavelength of 488 nm. Due to the high concentration of Ddx4-YFP even in the protein-lean phase, we first photobleached cells by acquiring a z-stack with high laser power. FCS experiments are performed with 30 s measurement time and data are fit to Eq. S29, resulting in $D_+ = 36$ +/- 11 µm^2/s (Fig. S16). In living cells, refractive index mismatch can further distort the FCS measurement volume. The nucleoplasm refractive index is estimated to be ~1.36 (12), which would lead to ~20% error in the diffusion coefficient (13).
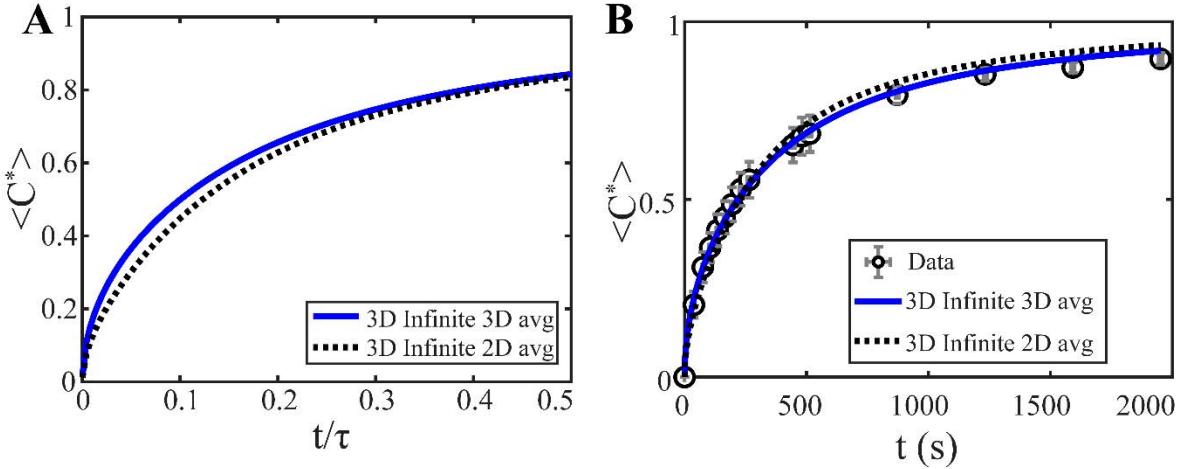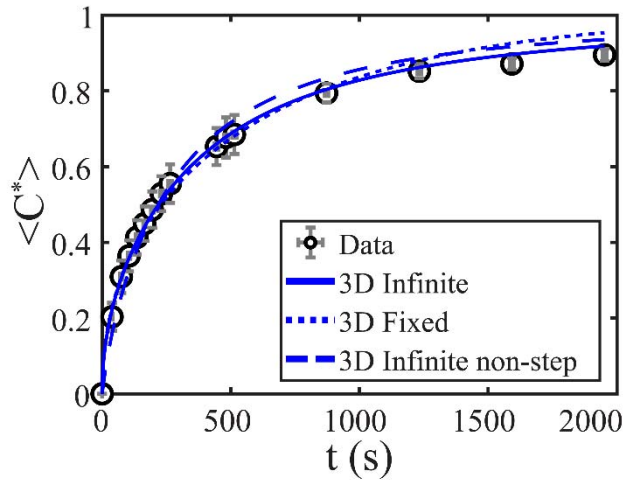
Supplementary Figures
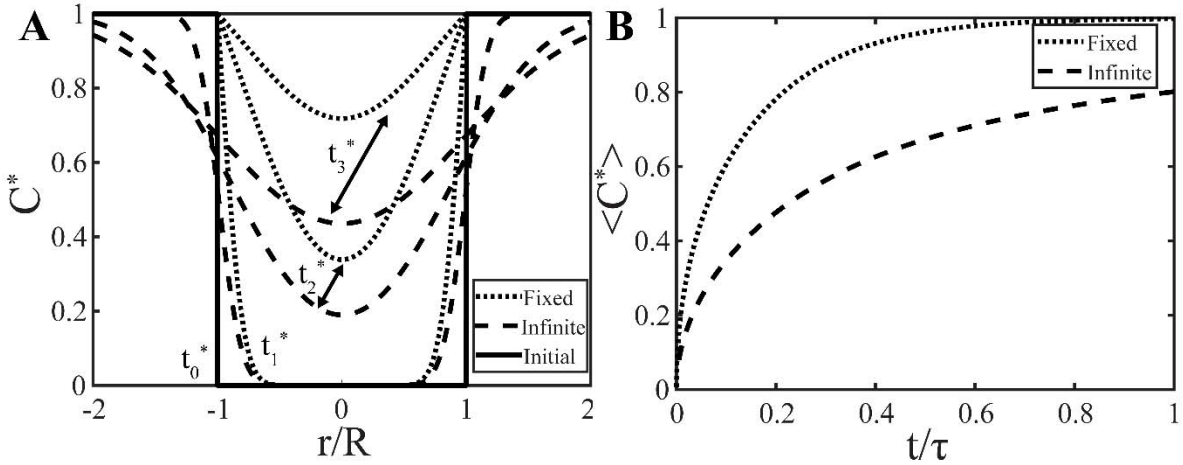
Supplementary Figure 1. (A) Calculated concentration profiles for 2D fixed (black dotted line) and infinite boundary (black dashed line) models for three time points with the initial concentration profile shown (solid-black line). Here, $t^* = t/\tau$ and $t_0^* = 0$, $t_1^* = 0.01$, $t_2^* = 0.15$, $t_3^* = 0.3$. (B) Calculated $<C^*>$ versus t/τ for 2D fixed (black dotted line) and infinite boundary (black dashed line) models. $\tau = R^2/D$ for both models.
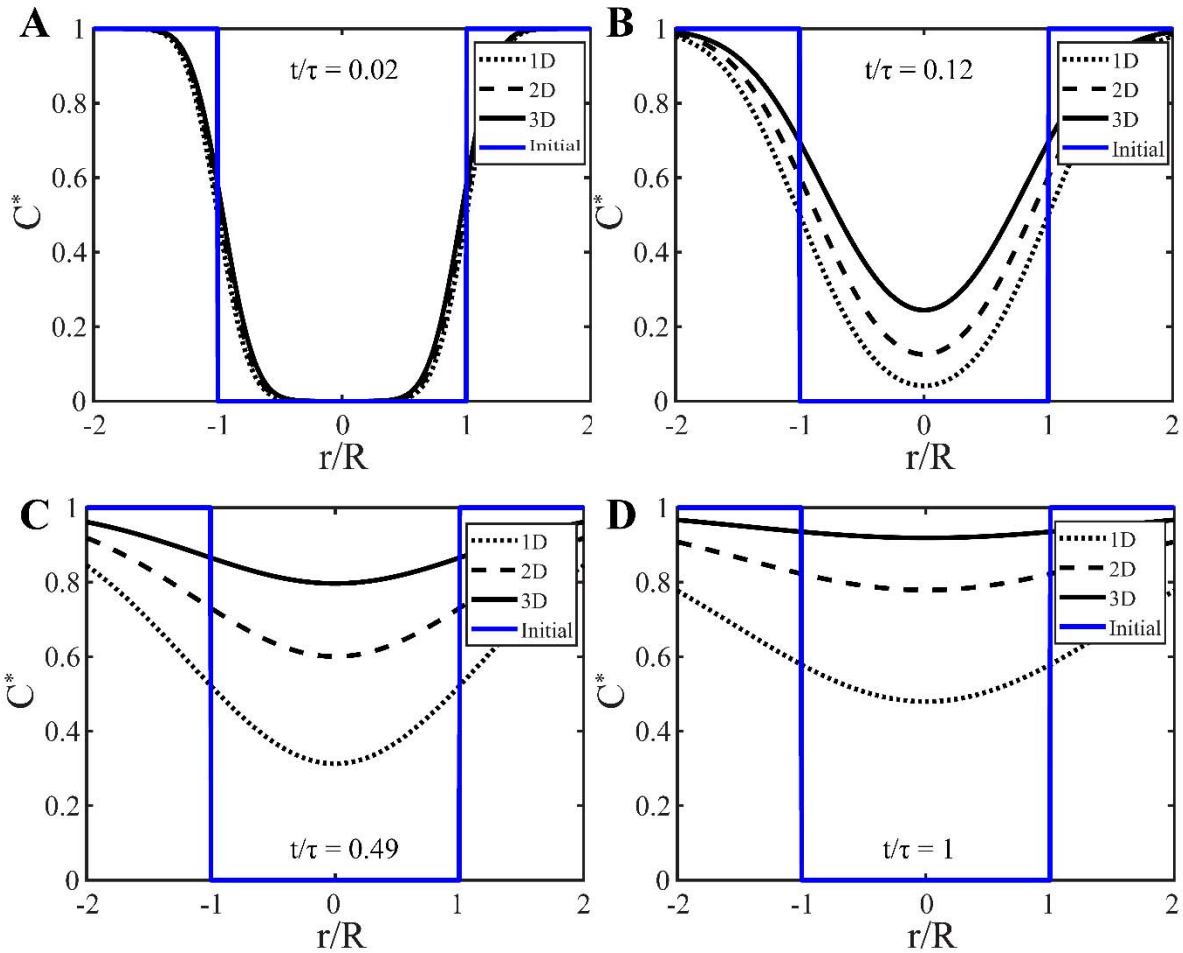
Supplementary Figure 2. Calculated concentration profiles for four time points for infinite boundary models in 1D (black dotted line), 2D (black dashed line), and 3D (black solid line). Initial profile is shown as blue solid line. (A) t/τ = 0.02, (B) t/τ = 0.12, (C) t/τ = 0.49, and (D) t/τ = 1.

Supplementary Figure 3. (A) Calculated $<C^*>$ versus t/τ for 3D Infinite model using a 3D average (blue solid line) and 2D average (black dotted line). (B) Measured $<C^*>$ versus t (black open circles) for LAF-1 using a ROI = 3 μm fit to the 3D infinite boundary model with step initial condition using a 3D average (blue solid line) or 2D average (black dotted line).

Supplementary Figure 4. Measured $<C^*>$ versus t (black open circles) for LAF-1 using a ROI = 3 μm fit to the 3D (blue solid line) infinite boundary model with step initial condition, 3D infinite boundary with non-step initial condition (blue dashed line), and 3D fixed boundary model (blue dotted line).
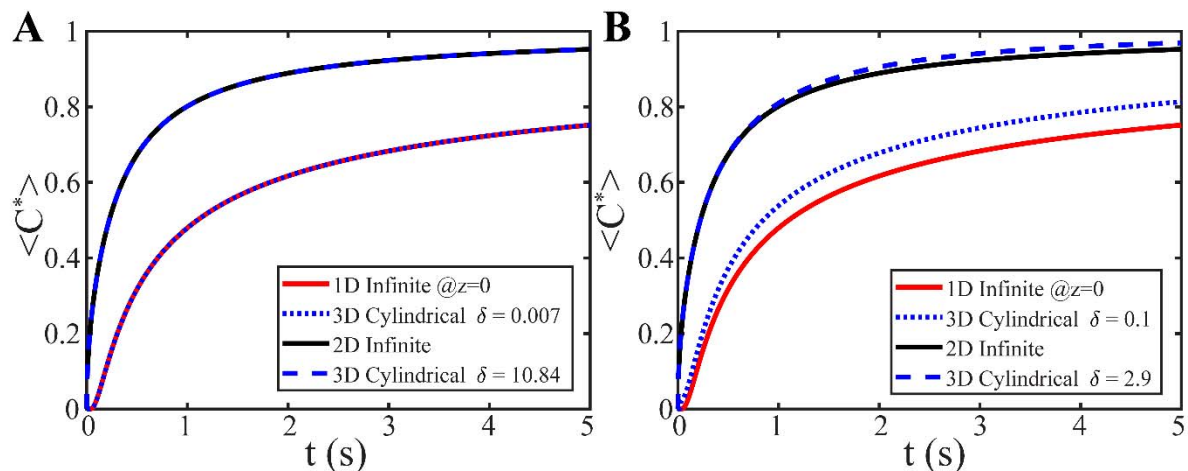
Supplementary Figure 5. (A) δ values required for 3D Cylindrical model to display quasi-1D (blue dotted line with δ = 0.007) or quasi-2D (blue dashed line with δ = 10.84) behavior reflected by $<C^*>$ vs t. (B) Comparison between 1D Infinite (red solid line) and 3D Cylindrical model (blue dotted line) using δ = 0.1 and 2D Infinite (black solid line) and 3D Cylindrical model (blue dashed line) using δ = 2.9, values characteristic of our experiments.
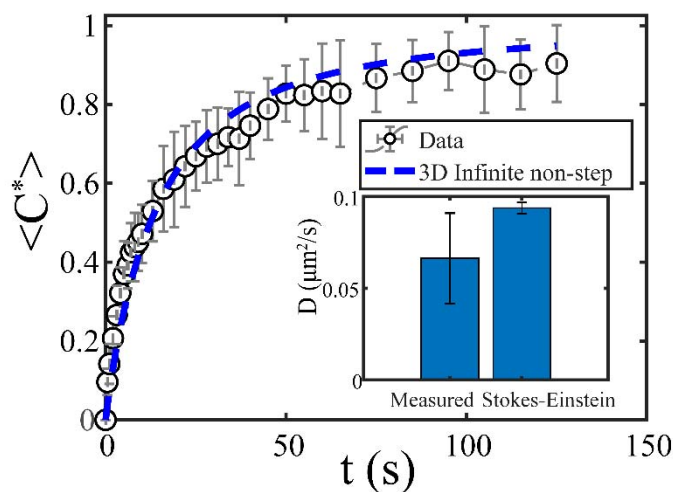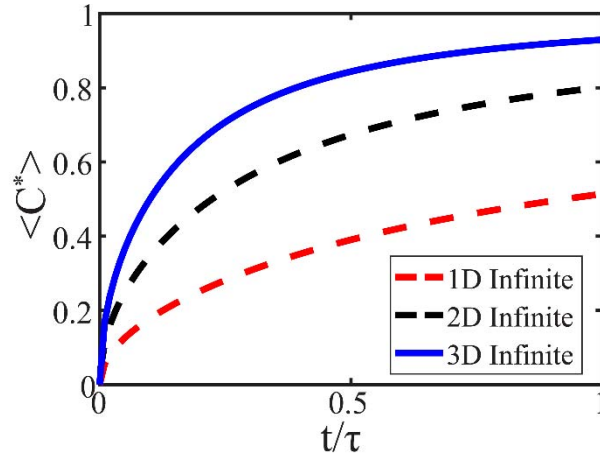

Supplemental Figure 6. Measured $<Ct(^*>$ versus t (black open circles) of 20 nm beads in 90% glycerol using a ROI = 2.5 μm fit to the 3D infinite boundary with non-step initial condition (blue dashed line). (Inset) Fitting to this model yields a similar diffusion coefficient to that expected from Stokes-Einstein (i.e., $D_{Stokes-Einstein}$ = 0.094 +/- 0.003 μm²/s vs D = 0.066 +/- 0.025 μm²/s). Typical error bars are shown and represent standard deviation of four replicates. Stokes-Einstein error bar corresponds to standard deviation of using the three literature reports of viscosity (see Supplementary text).
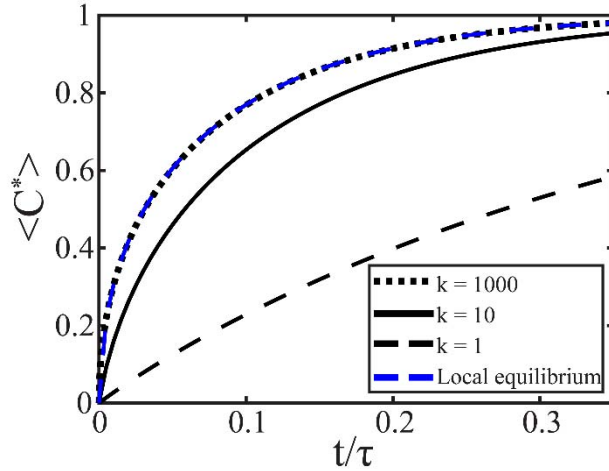
Supplemental Figure 7. Calculated $<C^*>$ versus t/τ for 3D finite model with local equilibrium assumption (blue dashed line) or interface resistance with $k = 1000$ (black dotted line), $k = 10$ (black solid line), and $k = 1$ (black dashed line). $\tau = R^2/D$ for both models.
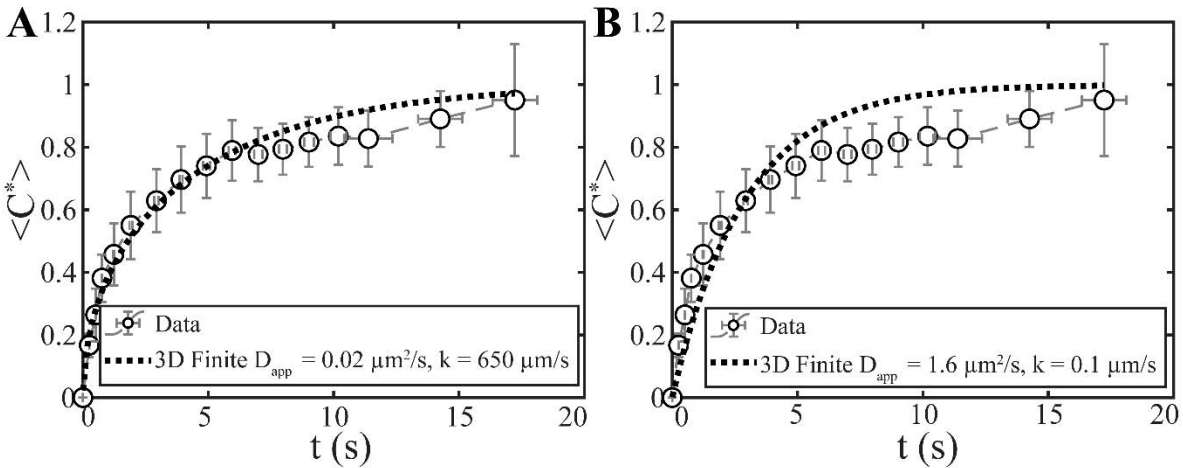

Supplemental Figure 8. FRAP data for Ddx4-YFP (open black circles) using $R_{drop}/R_{bleach} = 1$ fit using the 3D finite model accounting for interface resistance (dotted black line) results in (A) apparent $D = 0.023 \pm 0.009$ μm²/s and $k = 648 \pm 600$ μm/s, $R^2 = 0.98$. (B) Constraining the fit parameters results in a nearly as well fit ($R^2 = 0.86$) with $D = 1.56 \pm 0.68$ μm²/s and $k = 0.10 \pm 0.01$ μm/s. Typical error bars are shown and represent standard deviation of measurements on eight cells.

Supplementary Figure 9. Calculated $<C^*>$ versus t/τ for 1D (red dashed line), 2D (black dashed line), and 3D infinite (blue solid line) models with $\tau = R^2/D$ for all models.
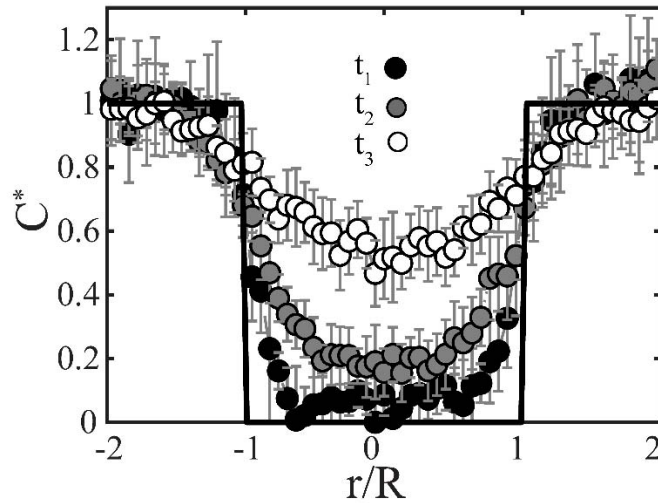

Supplemental Figure 10. Measured concentration profiles for LAF-1 in the xy plane for three time points demonstrate that C^* at $r/R = 1$ is not fixed at 1 using a ROI = 3 μm. Here, $t_1 = 0$ min, $t_2 \sim 1$ min and $t_3 \sim 4$ min after bleaching. Typical error bars are shown and represent standard deviation of eight replicates.
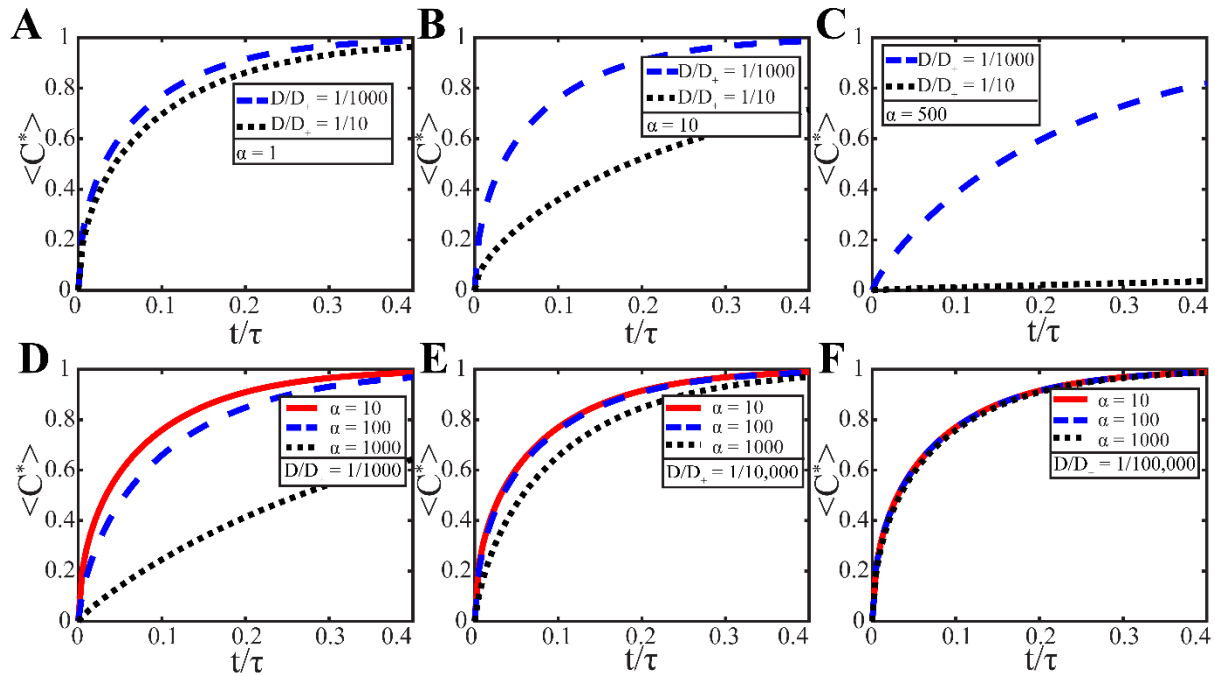
Supplemental Figure 11. Calculated $<C^*>$ versus t/τ for 3D finite model with (A) $\alpha = 1$, (B) $\alpha = 10$, and (C) $\alpha = 500$ with $D/D_+ = 1/1000$ (blue dashed line) and $D/D_+ = 1/10$ (black dotted line) demonstrates reduced sensitivity to D/D_+ for small α. $<C^*>$ versus t/τ for 3D finite model with (D) $D/D_+ = 1/1000$, (E) $D/D_+ = 1/10,000$, and (F) $D/D_+ = 1/100,000$ with $\alpha = 10$ (red solid line), $\alpha = 100$ (blue dashed line), and $\alpha = 1000$ (black dotted line) demonstrates reduced sensitivity to α for small D/D_+.
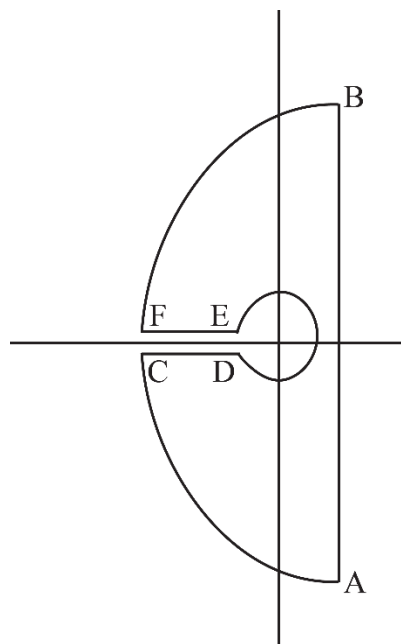
Supplemental Figure 12. Contour with a cut along the negative real axis used to calculate the integral in Eq. S20-S21 (3).
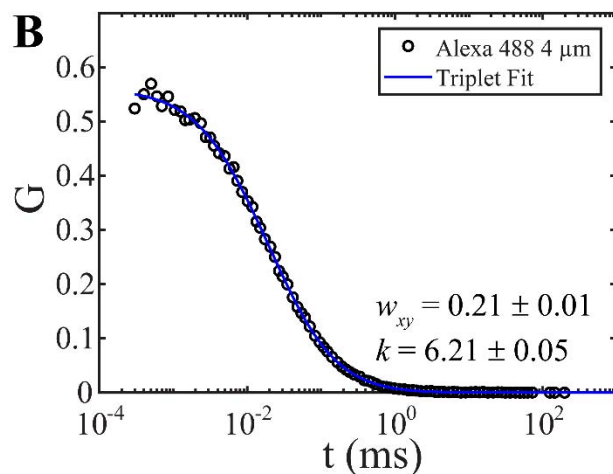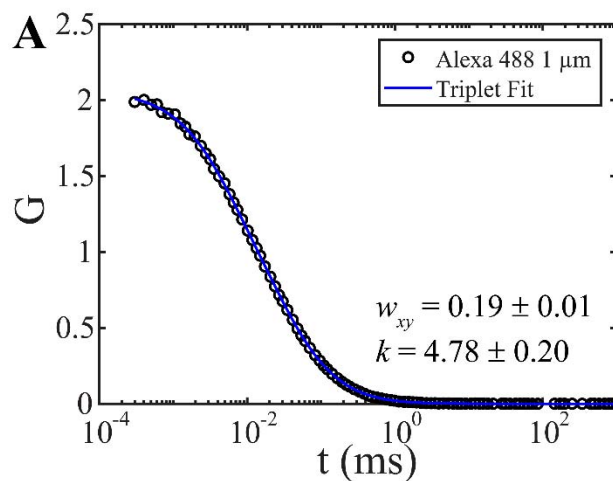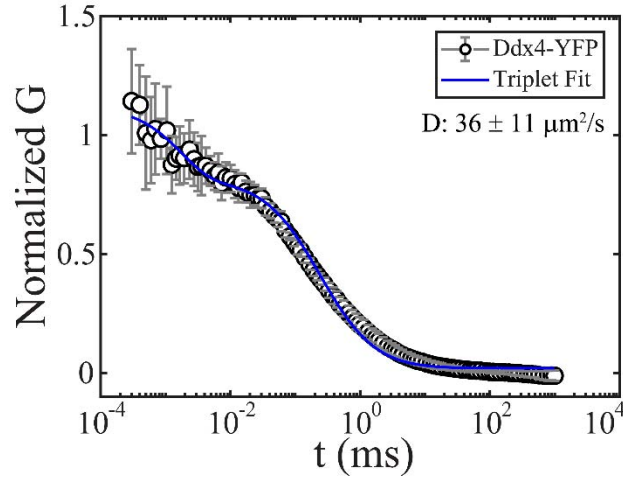

Supplemental Figure 13. (A) Autocorrelation curve obtained 1 μm above the coverslip for a 10 nM Alexa488 solution fit to Eq. S29 results in $w_{xy} = 0.19 \pm 0.01$ and $k = 4.78 \pm 0.20$. (B) Autocorrelation curve obtained 4 μm above the coverslip for a 10 nM Alexa488 solution fit to Eq. S29 results in $w_{xy} = 0.21 \pm 0.01$ and $k = 6.21 \pm 0.05$.
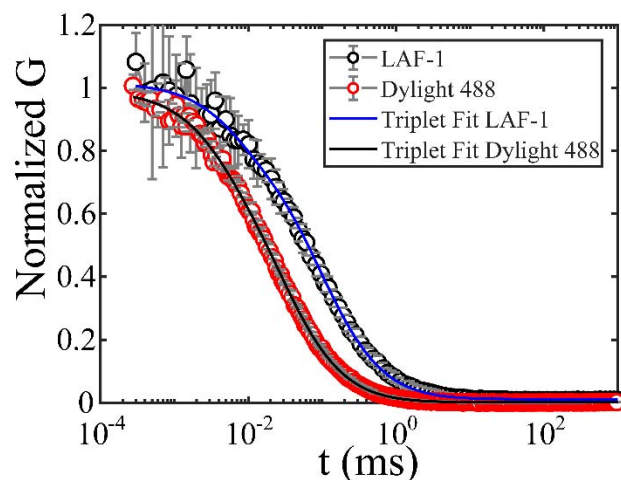
Supplemental Figure 14. Normalized autocorrelation curve obtained 4 μm above the coverslip in the protein-lean phase of a LAF-1 80 mM NaCl solution (black open circles) and of Dylight 488 (red open circles). Data are fit to Eq. S29 using $k = 4.78$ +/- 0.20 and $w_{xy} = 0.19$ +/- 0.01. Fitting using $k = 6.21$ +/- 0.05 and $w_{xy} = 0.21$ +/- 0.01 results in a 39% decrease and 28% increase in C_∞ and D, respectively. Typical error bars are shown and represent standard deviation of five replicates.
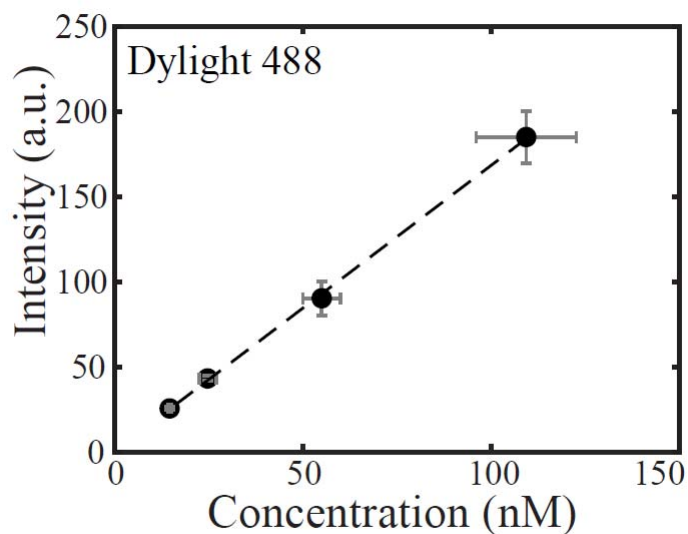
Supplemental Figure 15. Dylight 488 fluorescence to concentration calibration curve obtained 4 μm above the coverslip of a Dylight488 solution using fluorescence correlation spectroscopy. Concentration is calculated using $k = 4.78$ +/- 0.20 and $w_{xy} = 0.19$ +/- 0.01. Typical error bars are shown and represent standard deviation of three replicates.

Supplemental Figure 16. Autocorrelation curve obtained 1 μm above the coverslip of Ddx4-YFP in Hek293 cell nuclei. Data are fit to Eq. S29 using $k = 4.78$ +/- 0.20 and $w_{xy} = 0.19$ +/- 0.01. Typical error bars are shown and represent standard deviation (n = 15 cells).
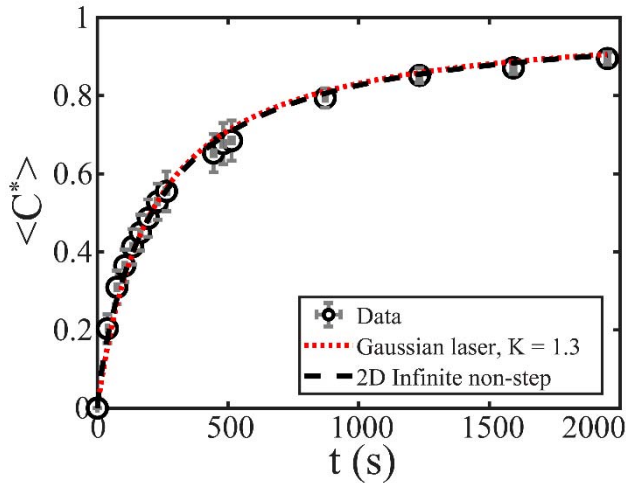
Supplemental Figure 17. Measured $<C^*>$ versus t (black open circles) for LAF-1 using a ROI = 3 μm fit to the 2D infinite boundary model with non-step initial condition (black dashed line) and Eq. 12 in Axelrod et al. (14) with K = 1.3 found using Eq. 7 in Axelrod et al. (14). Diffusivities estimated using both models (i.e., Eq. 12 in Axelrod et al. (14) and 2D infinite non-step) are 0.0034 and 0.0035 $\mu m^2/s$, respectively.

Supporting References

1. Crank, J. 1975. The Mathematics of Diffusion. Second. Oxford University Press.

2. Sprague, B.L., R.L. Pego, D.A. Stavreva, and J.G. McNally. 2004. Analysis of Binding Reactions by Fluorescence Recovery after Photobleaching. Biophys. J. 86: 3473–3495.

3. Carslaw, H.S., and J.C. Jaeger. 1959. Conduction of Heat in Solids. Second. Oxford:

Clarendon Press.

4.   Penkova, A., K. Rattanakijsuntorn, S.S. Sadhal, Y. Tang, R. Moats, P.M. Hughes, M.R. Robinson, and S.S. Lee. 2014. A technique for drug surrogate diffusion coefficient measurement by intravitreal injection. Int. J. Heat Mass Transf. 70: 504–514.

5.   Cooper, F. 1976. Heat Transfer from a Sphere to an Infinite Medium. Int. J. Heat Mass Transf. 20: 991–993.

6.   Scott, E.J., L.H. Tung, and H.G. Drickamer. 1951. Diffusion through an interface. J. Chem. Phys. 19: 1075–1078.

7.   Segur, J.B., and H.E. Oderstar. 1951. Viscosity of Glycerol and Its Aqueous Solutions. Ind. Eng. Chem. 43: 2117–2120.

8.   Petrášek, Z., and P. Schwille. 2008. Precise Measurement of Diffusion Coefficients using Scanning Fluorescence Correlation Spectroscopy. Biophys. J. 94: 1437–1448.

9.   Banachowicz, E., A. Patkowski, G. Meier, K. Klamecka, and J. Gapiński. 2014. Successful FCS experiment in Nonstandard Conditions. Langmuir. 30: 8945–8955.

10.   Enderlein, J., I. Gregor, D. Patra, T. Dertinger, and U.B. Kaupp. 2005. Performance of Fluorescence Correlation Spectroscopy for Measuring Diffusion and Concentration. ChemPhysChem. 6: 2324–2336.

11.   Wei, M.-T., S. Elbaum-Garfinkle, A.S. Holehouse, C.C.-H. Chen, M. Feric, C.B. Arnold, R.D. Priestley, R. V Pappu, and C.P. Brangwynne. 2017. Phase behaviour of disordered proteins underlying low density and high permeability of liquid organelles. Nat. Chem. 9: 1118–1125.

12.   Choi, W., C. Fang-Yen, K. Badizadegan, S. Oh, N. Lue, R.R. Dasari, and M.S. Feld. 2007. Tomographic phase microscopy. Nat. Methods. 4: 717–719.

13.   Bracha, D., M.T. Walls, M.-T. Wei, L. Zhu, M. Kurian, J.L. Avalos, J.E. Toettcher, and C.P. Brangwynne. 2018. Mapping Local and Global Liquid Phase Behavior in Living Cells Using Photo-Oligomerizable Seeds. Cell. 175: 1467-1480.e13.

14.   Axelrod, D., D.E. Koppel, J. Schlessinger, E. Elson, and W.W. Webb. 1976. Mobility Measurement by Analysis of Fluorescence Recovery Kinetics. Biophys. J. 16: 1055–1069.